Amorphous to Crystal Conversion as a Mechanism Governing the Structure of Luminescent YVO_4:Eu Nanoparticles

Blaise Fleury,[†,‡,⊥] Marie-Alexandra Neouze,[†,‡] Jean-Michel Guigner,[§] Nicolas Menguy,[§] Olivier Spalla,[‡,⊥] Thierry Gacoin,[†,⊥] and David Carriere[‡,⊥,*]

[†]Groupe de Chimie du Solide, Laboratoire de Physique de la Matière Condensée, UMR CNRS 7643, École Polytechnique, 91128 Palaiseau, France, [‡]CEA Saclay, IRAMIS, UMR CEA/CNRS 3299 SIS2M, 91191 Gif sur Yvette, France, and [§]Institut de Minéralogie, de Physique des Matériaux, et de Cosmochimie (IMPMC) Sorbonne Universités - UPMC Univ Paris 06, UMR CNRS 7590, Muséum National d'Histoire Naturelle, IRD, UMR 206, 4 Place Jussieu, F-75005 Paris, France. [⊥]These authors contributed equally.

ABSTRACT The development of functional materials by taking advantage of the physical properties of nanoparticles needs an optimal control over their size and crystal quality. In this context, the synthesis of crystalline oxide nanoparticles in water at room temperature is a versatile and industrially appealing process but lacks control especially for "large" nanoparticles (>30 nm), which commonly consist of agglomerates of smaller crystalline primary grains. Improvement of these syntheses is hampered by the lack of knowledge on possible intermediate, noncrystalline stages, although their critical importance has already been outlined in crystallization processes. Here, we show that during the synthesis of luminescent Eu-doped YVO_4 nanoparticles a transient amorphous network forms with a two-level structuration. These two prestructuration scales constrain topologically the nucleation of the nanometer-sized crystalline primary grains and their aggregation in nanoparticles, respectively. This template effect not only clarifies why the crystal size is found independent of the nucleation rate, in contradiction with the classical nucleation models, but also supports the possibility to control the final nanostructure with the amorphous phase.

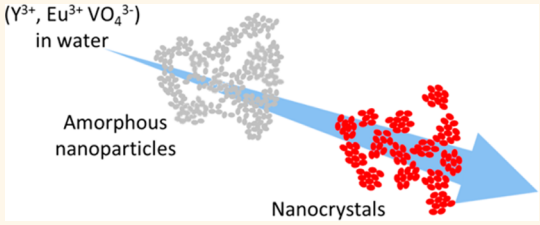

KEYWORDS: nanoparticles · nucleation · biomineralization · SAXS · WAXS · luminescence · YVO_4

The physical properties of nanoparticles are determined by a balance between effects brought by size reduction and by their crystalline structure.[1,2] Controlling simultaneously not only the size but also the quality and type of crystal is therefore a fundamental issue at the root of many aspects in nanosciences. In this context, understanding the formation of nanocrystals becomes especially crucial regarding syntheses of oxide nanoparticles in aqueous solution and at room temperature. Indeed, the syntheses of oxides by "soft chemistry" involve a variety of reactions between the precursor metal ions and water or hydroxyl groups (*e.g.*, hydrolysis, condensation, olation, oxolation), leading to numerous possible metastable chemical and structural intermediates.[3] In particular, there are numerous examples of "large" oxide nanoparticles (>30 nm) made of agglomerates of smaller crystalline primary grains, which therefore require thermal annealing to favor coalescence into single nanocrystals.[4−9]

The syntheses of crystalline oxide nanoparticles are therefore good candidates to elucidate the relation between the possible intermediate states and the final nanocrystals. In particular, the complexity of the reaction provides a favorable ground to tackle the cases where the nucleation of the nanoparticles deviate strongly from the so-called "classical nucleation theory". This empirical description of nucleation assumes indeed that concentration fluctuations in the precursor solution lead to nuclei which already show the final crystalline structure.[10] However, the quantitative failure of this description has outlined the critical role of intermediate states:[11] following a principle of least effort, concentration fluctuations would lead first to liquid dense intermediates (regions more concentrated in solutes), from which the crystals would then nucleate after structural order fluctuations. The observation of intermediate stages is however hampered by the lack of space and time resolution: calcium carbonate

* Address correspondence to david.carriere@cea.fr.

Received for review December 5, 2013 and accepted February 8, 2014.

Published online February 08, 2014
10.1021/nn4062534

and phosphate are the rare systems where cryo-TEM has allowed imaging stable prenucleation clusters[12] and their subsequent aggregation into nanoparticles.[13,14] Inversely, the coalescence of primary nanocrystals of magnetite into single nanoparticles has been captured but not the formation of the primary crystals themselves.[15]

Here, we elucidate the formation of luminescent Eu-doped YVO_4 nanoparticles from aqueous ionic precursors. *In situ* X-ray scattering and fluorescence techniques allow following the formation of the nanocrystals in the 0.5 s to 1 h range, with subsecond time resolution. We demonstrate the formation of a transient amorphous network which already shows two characteristic sizes in the nanometer range and following the relation between this prestructuration and the final nanoparticles after crystallization. This not only elucidates why the crystal size is found independent of the nucleation rate, in contradiction with the classical mechanisms of ion-by-ion formation,[10,16−18] but also supports the possibility to control the final nanostructure with the amorphous phase.

RESULTS

To tackle this problem, we have used as a model experimental system the synthesis in aqueous solution of luminescent Eu-doped YVO_4 nanoparticles. Characterizations by transmission electron microscopy (Cryo-TEM and HRTEM, Figure 1a−d) and by small- and wide-angle X-ray scattering (SAXS/WAXS, Figure 1e) both reveal that the final nanoparticles have a mean diameter of 40 nm and are themselves composed of crystalline primary grains with a mean diameter of 2 nm. At larger scattering angles, the (101), (200), and (112) Bragg peaks of the YVO_4:Eu crystalline phase are identified. This two-scale morphology (nanoparticles made of smaller crystalline primary grains) is representative of that of other nanoparticles synthesized in aqueous solution such as TiO_2, ZrO_2 (Figure 1f,g and Supporting Information 1), YAG, ZnO, or CeO_2.[4−9] Furthermore, electron diffraction demonstrates that, in the final YVO_4:Eu nanoparticles, the (200) and ($1\bar{1}2$) planes propagate at the scale of several crystalline primary grains (Figure 1c,d). Although electron diffraction data are not available for all other above-mentioned oxides, we note that this property has been reported for some ZrO_2 syntheses[6] and numerous biominerals.[19] Looking for a possible common formation process, we considered Eu-doped YVO_4 as a convenient model system since (i) the red luminescence of the Eu(III) ions upon transfer of UV excitation from the YVO_4 matrix is a convenient probe for the quality of the crystalline lattice (Figure 1h), (ii) the nanostructure determines strongly the physical properties.[20] These nanoparticles are used as precursors for thin transparent luminescent films or as biological probes.[21−24] For these nanoparticles, the *multiscale* nanostructure

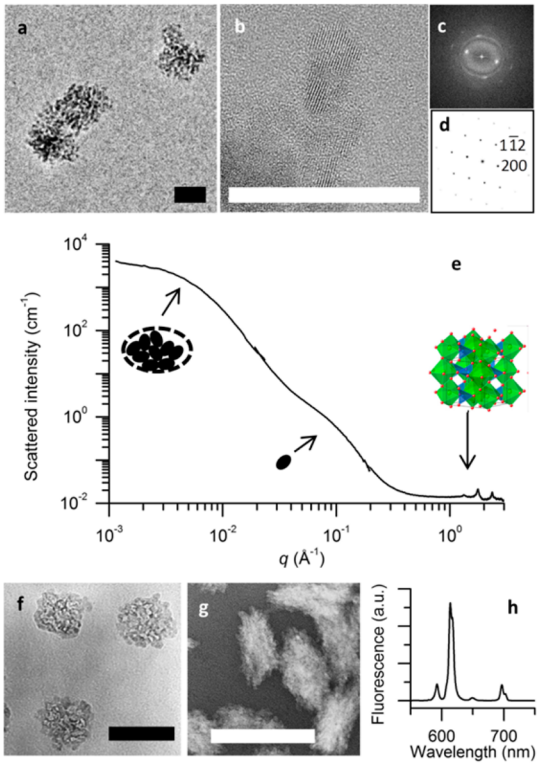

Figure 1. Characterization of multiscale nanoparticles. (a) Cryo-TEM pictures of Eu-doped YVO_4 nanoparticles (scale bar: 25 nm). (b−d) HRTEM of a single nanocrystal observed along a [021] zone axis with the corresponding FFT and the calculated diffraction pattern (scale bar: 25 nm). (e) Corresponding small- and wide-angle X-ray scattering patterns in solution. The crossover regime at $q = 10^{-2}$ Å^{-1} is assigned to the size of the nanoparticles ($\langle d \rangle = 30$ nm), and the crossover regime at $q = 1.5 \times 10^{-1}$ Å^{-1} to the primary grains ($\langle d \rangle = 2$ nm). (f,g) TEM pictures of TiO_2 and ZrO_2 nanoparticles (scale bars: 50 nm). (h) Fluorescence spectrum of a YVO_4:Eu nanoparticle solution excited at 280 nm.

determines the luminescence response of each individual nanoparticle through the efficiency of surface interactions (which enhances sensitivity to probe solutes), the effective dielectric constant of each nanoparticle, the number of active Eu(III) emitting centers per nanoparticle, and the crystal quality of the primary grains which controls the efficiency of the excitation transfer from the YVO_4 matrix to the Eu(III) emitting centers.[20,25]

The nanoparticles are synthesized by coprecipitation, mixing (i) an aqueous solution of yttrium and europium nitrates and (ii) an aqueous solution of sodium orthovanadate at pH = 12.5.[26] Upon addition of the yttrium−europium solution, the clear vanadate solution turns white and turbid. After typically 1 h of reaction, an aqueous dispersion of crystalline, luminescent Eu-doped YVO_4 nanoparticles is obtained. In order to elucidate the formation of both characteristic sizes and their emergence from the homogeneous reactive solutions, we have followed the syntheses by *in situ* time-resolved SAXS/WAXS coupled with fluorescence spectroscopy (Figure 2 and Figure 3). SAXS/WAXS allows probing the correlations in electron densities

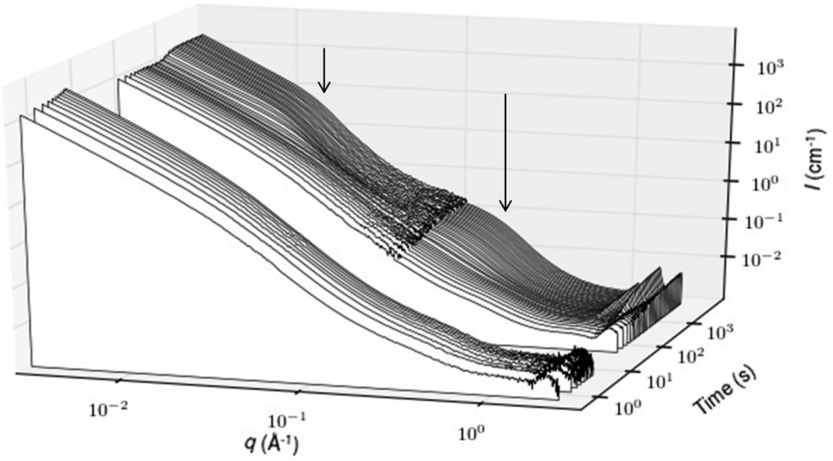

Figure 2. Time-resolved small- and wide-angle X-ray scattering of the aqueous solution during the formation of the nanoparticles. The emergence of the crossover regimes at $q = 10^{-2}$ Å^{-1} and $q = 1.5 \times 10^{-1}$ Å^{-1} (arrows) is the signature of the formation of the crystalline primary grains and nanoparticles, respectively. See also Supporting Information 5.

over 3 orders of magnitude in distances, down to the angstrom, in a millimeter-sized sample of liquid (containing typically 10^{11} nanoparticles) without specific preparation. Our setups achieve a time resolution of 100 ms for reaction times below 4 s and a time resolution of 2 s for reaction times above 4 s (see Methods). After mixing the precursors, the scattered intensity expressed as a function of the wavevector $q = 4\pi/\lambda \sin \theta$, where θ is half the scattering angle, presents two characteristic features which are observed between the shortest measurable time ($t \approx 400$ ms) and a reaction time of 2 min: (i) at small angles, an increase of the scattered intensity by more than a factor of 10^6 with respect to the precursors (Figure 2 and Supporting Information 2), characteristic of large ($d > 100$ nm) structures; (ii) a broad signal at $q = 2$ Å^{-1} (Figure 3a). This broad signal is assigned to the formation of an amorphous phase, that is, a phase which lacks translational order beyond distances estimated to $2\pi/\Delta q = 0.5$ nm (with Δq the full width at half-maximum of the peak). The SAXS/WAXS patterns therefore demonstrate that an amorphous network forms faster than 400 ms.

We highlight that the decay of the scattering intensity with q is not featureless (Figure 2 and Supporting Information 2). Instead, two broad oscillations are observed, centered at $q = 4 \times 10^{-2}$ and 4×10^{-1} Å^{-1}, respectively, which unveil that this transient amorphous network shows two characteristic sizes. The sizes of these structures are determined by fitting the SAXS pattern with the so-called unified equation[27] (Supporting Information 3), which describes a three-level organization (nanometer-size structures, which are organized into larger structures, themselves organized into bigger aggregates). We find that the smaller structures present a radius of gyration of 0.5 nm, agglomerated into bigger aggregates with a radius of gyration of 14 nm. Both structures are directly observable by transmission electron microscopy in mixtures of precursors quenched in liquid ethane after 56 s of reaction (cryo-TEM, Figure 4). The smaller size ($q = 0.4$ Å^{-1}) is assigned to nanometer-sized elementary clusters (Figure 4b), which are organized into fractal aggregates. The larger size ($q = 0.04$ Å^{-1}) is assigned to the section of the fractal aggregates (Figure 4a). Furthermore, the size of the elementary clusters coincides with the coherence distance estimated from the width of the WAXS pattern (0.5 nm). This suggests that the amorphous network may consist of identical clusters, which only lack mutual orientational order (as opposed to a network which consists of clusters which show structural disorder, *i.e.*, distribution in bond angles and lengths). As the WAXS pattern in the 1−3 Å^{-1} range is not consistent with the calculated pattern for small YVO_4 crystals, even as small as 0.5 nm in radius (Supporting Information 4), we discard the situation where the elementary clusters would be YVO_4 units which already show the structure of the final crystal. Instead, the formation of the final nanoparticles must involve some local structural rearrangements in the amorphous network below the 0.5 nm scale.

During the first 2 min of reaction, no Bragg peak assigned to YVO_4 at $q > 1$ Å^{-1} is observed, which indicates the absence of nanocrystal formation (Figure 2 and Figure 3a). After an induction time of 135 s, three simultaneous evolutions in the SAXS/WAXS patterns are observed (Figure 2, Figure 3a, and Supporting Information 5): (i) The signal assigned to the atomic-range correlations in the amorphous phase ($q = 2$ Å^{-1}) vanish, while the intensity of the Bragg peaks of the YVO_4:Eu crystals increases. This shows the progressive conversion of the amorphous network into crystalline nanoparticles. Accordingly, the fluorescence intensity increases (Figure 3b) as the excitation transfer from the YVO_4 matrix to the Eu(III) ions is enhanced. (ii) The scattering assigned to the elementary clusters decreases ($q = 4 \times 10^{-1}$ Å^{-1}, Figure 2), while the intensity assigned to the scattering by the crystalline

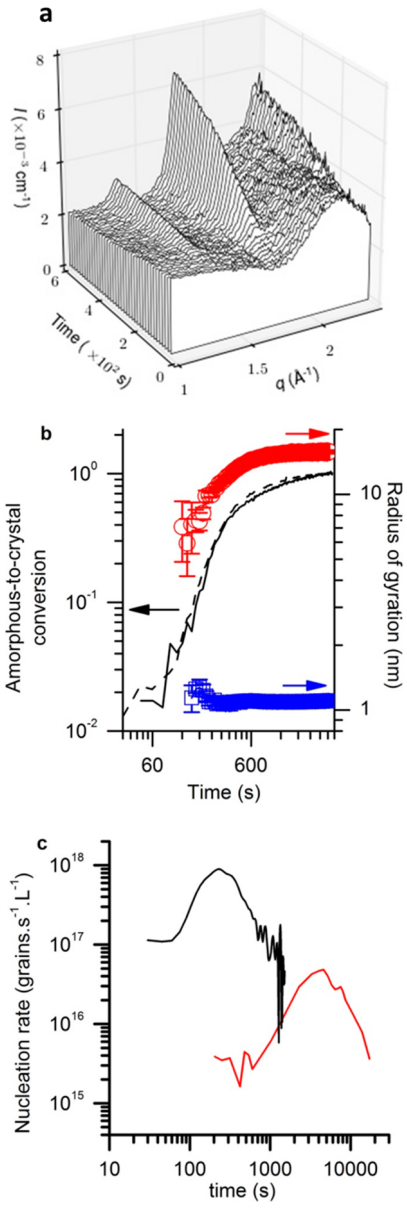

Figure 3. Evolution of the primary crystalline grains with time. (a) Zoom of the SAXS/WAXS patterns above 1 Å^{-1}. (b) Total luminescence intensity upon excitation at 280 nm and integrated between 550 and 730 nm (—) and intensity of the (200) reflection observed at q = 1.7 Å^{-1} (- - -), both normalized with respect to the value obtained at 62 min 15 s. Radius of gyration of the primary grains (blue) and of the nanoparticles (red) from the fit of the SAXS/WAXS patterns as indicated in the text and Supporting Information 3. For clarity, only one symbol out of 10 is plotted. Error bars are 99% confidence intervals for the fits (see Supporting Information 3). (c) Nucleation rate of the primary crystalline grains for the synthesis at pH = 12.5 (top) and at pH = 13 (bottom). Upon increase of pH, the maximum nucleation rate is divided by a factor of 20, whereas the crystal size remains constant within experimental error.

primary grains increases (q = 2 × 10^{-1} Å^{-1}, Figure 2, right arrow and Supporting Information 5). (iii) The broad oscillation assigned to the agglomerates of elementary clusters (q = 4 × 10^{-2} Å^{-1}) shifts to smaller q values until the scattering assigned to the

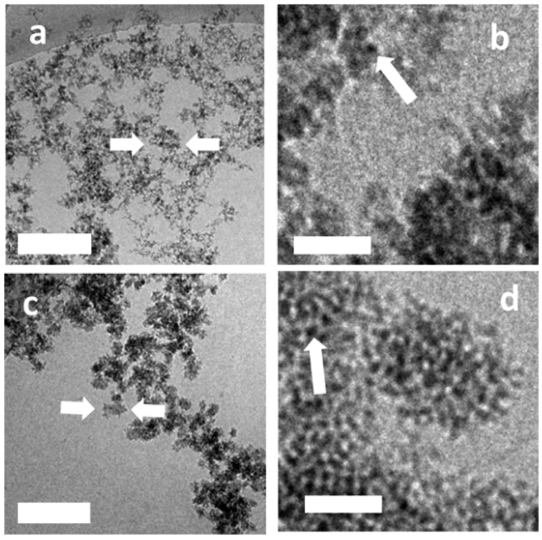

Figure 4. Cryo-TEM pictures of precursor mixtures quenched after (a) 56 s (scale bar: 200 nm); the arrows indicated the larger-scale prestructuration of the amorphous phase; (b) 56 s (scale bar: 20 nm); the arrow indicate one elementary cluster; (c) 32 min (scale bar: 200 nm); the arrows indicate a formed nanoparticle: (d) 32 min (scale bar: 20 nm); the arrow indicates a primary crystalline grain.

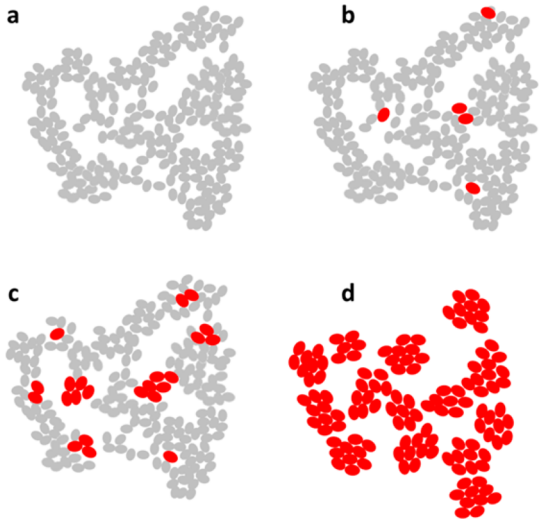

Figure 5. Proposed illustration of the structure evolution during the amorphous-to-crystal conversion of the nanoparticles. Gray oval: elementary clusters. Red ovals: luminescent crystalline primary grains.

nanoparticles is observed (q = 1.5 × 10^{-2} Å^{-1}, Figure 2, left arrow and Supporting Information 5).

This qualitative survey of the SAXS data proves the progressive conversion of the amorphous, structured network into crystalline primary grains and nanoparticles (Figure 5). Cryo-TEM obtained after 32 min of reaction confirms the formation of a large-scale network of crystalline nanometer-sized primary grains, where the 40 nm nanoparticles emerge as substructures (Figure 4c,d). A quantitative treatment of the scattering data highlights how the prestructured amorphous phase determines the final sizes of the

nanoparticles (Supporting Information 3). For each reaction time, the SAXS pattern ($q < 1$ Å^{-1}) of the already crystallized nanoparticles is extracted after subtraction of the appropriate fraction of the amorphous phase, as evaluated from the WAXS part ($q > 1$ Å^{-1}) by fitting the pattern with a linear combination of a reference pattern of the amorphous phase (taken at $t = 15$ s) and of the crystalline nanoparticles ($t = 62$ min 15 s). This signal extraction allows fitting the SAXS pattern of the nanoparticles alone with the three-level unified equation[27] as above (Supporting Information 3) to capture the organization of the crystalline primary grains into nanoparticles and the aggregation of nanoparticles into larger structures. The treatment of the WAXS and SAXS data therefore provides (i) the progress of the amorphous-to-crystal conversion, which is in good agreement with the evaluation obtained independently by the fluorescence intensity, and (ii) the characteristic sizes of the already formed primary grains and nanoparticles (Figure 3b).

As a result from fitting SAXS data restricted to the formed particles with the unified equation, we find that the mean radius of the nanoparticles made of the crystalline primary grains progressively increases with time (Figure 3b). This reflects that the mean number of crystalline grains which are aggregated into nanoparticles increases (Figure 5b,c). We observe that the larger characteristic size of the amorphous network (15 nm) is preserved during the crystallization (Figure 2 and Figure 4). It suggests that the amorphous network templates the larger-scale organization of the primary grains into nanoparticles and their aggregation into even larger-scale structures (aggregates of nanoparticles, Figure 4c,d). The number of primary grains per nanoparticles (here, on the order of 1000) is therefore constrained by the characteristic sizes of the amorphous network in which the primary crystalline grains form.

At smaller scales, we find that the size of the crystalline primary grains remains constant ($R_g = 1.1$ nm, *i.e.*, a volume estimated to 5.6 nm^3, Figure 3b) at about twice the size of the elementary clusters (0.5 nm, *i.e.*, 0.5 nm^3). This supports that the crystalline primary grains follow a "popcorn" formation process: about 10 clusters convert into a crystalline primary grain, which amounts to about 70 YVO_4 units (0.08 nm^3 per unit from the crystallographic data of YVO_4), with no further growth. We observe that crystalline growth remains confined to a few nanometer-sized primary grains, instead of propagating in the continuous amorphous network. Furthermore, the nucleation rate of crystalline primary grains may be decreased by more than 1 order of magnitude without changing their final size (Figure 3c): reactions conducted at higher pH increase the induction time to 25 min (instead of 2 min) and decrease and delay the maximum nucleation rate ($r_{max} = 4 \times 10^{16}$ primary crystalline grains per second and per liter of reactive solution at 75 min, compared to 9×10^{17} s^{-1} L^{-1} at 4 min; also see details in Supporting Information 6). This slowing by a factor of 20 leaves the size of the elementary clusters and of the primary crystalline grains unaltered within experimental resolution (0.5 and 1.2 nm, respectively, as measured by SAXS).

DISCUSSION

The independence of nucleation rate with final size demonstrates that the buildup of the crystalline structural order in the dense amorphous network is not determined by usual diffusion- or reaction-limited schemes, which invoke explicitly the rate of conversion to account for the final size of the object.[11] We also discard size limitation by accumulation of electrostatic charge,[28] as the size is found independent of pH and ionic strength. Instead, we prove that the size of the final crystalline primary grain is determined by local, short-range effects. We postulate that the size limitation of the crystals at the nanometer scale is the signature of topological constraints: the formation of the nanocrystals does not follow an atom-by-atom scheme but involves local reorganization within the elementary clusters. The activation barrier becomes too high if the orientation mismatch between the already formed crystalline lattice and the neighboring clusters is too important. The nanometer-sized prestructuration of the amorphous phase therefore determines the size of the crystalline primary grain, by constraining the propagation of the crystalline order.

The elementary clusters that build the amorphous network are characterized by their size in the SAXS regime (*via* the electron density contrast between the cluster and the solvent) and in the WAXS regime (*via* the coherence size). The clusters are therefore individually present in the amorphous network and do not coalesce into a larger amorphous particle, as does, for example, calcium phosphate after hydrolysis of the so-called nanometer-sized "Posner clusters" ($Ca_9(PO_4)_6$).[29] As discussed above, WAXS data demonstrate that the clusters do not already show the structure of the final YVO_4 nanoparticles (see Supporting Information 4). Furthermore, it is observed that the WAXS pattern of the amorphous network is similar to that of the vanadate precursor solution (Figure 3a and Supporting Information 2). In the experimental conditions used for the synthesis (pH = 12.5, [V] = 0.1 mol/L), the predominant species in the vanadate precursor is expected to be the pyrovanadate dimer $V_2O_7^{4-}$.[30] This is supported, although indirectly, by the similarity between the experimental WAXS pattern and the calculated WAXS pattern for clusters of crystalline $K_4V_2O_7$ containing eight V atoms (*i.e.*, four pyrovanadates; see Supporting Information 4). It finally suggests that the pyrovanadate precursors may contribute significantly to the structure of the amorphous network.

The structural buildup by reorientation of a less ordered phase is invoked in the so-called "nonclassical", two-step nucleation mechanism:[11] following a principle of least effort, this nucleation model states that the crystalline phase nucleates from a disordered intermediate dense phase, instead of nucleating directly from the solution. Two different types of dense liquid intermediate phases have been proposed:[11] either a liquid−liquid phase separation, as observed by simulation in $CaCO_3$ solutions,[31] or liquid-like prenucleation clusters, as observed experimentally in $CaCO_3$ solution under saturation.[12] We propose that the formation of the amorphous network observed here follows the same principle of least effort: the transient liquid dense intermediate phases preferably form in this case a dense amorphous network, instead of nucleating directly the crystalline phase. The amorphous phase appears as a possible generic additional intermediate on the way from metal ions to crystalline nanoparticles, and we anticipate future theoretical and experimental studies with sufficient time resolution will consolidate this universal character in metal phosphates or simple oxides synthesized in water. Beyond the interest for synthetic functional nanomaterials, this investigation of YVO_4:Eu nanoparticles is relevant for the fundamental understanding of biomineralization. The decoupling between the final shape—dictated by that of the amorphous phase—and crystal properties at the nanometer scale is indeed identified as advantageous in evolutionary processes.[19] Here, we bring a direct demonstration of the independence between the nucleation rate and the final crystal size and morphology and outline that the constitutive clusters of the amorphous network do not coalesce into a continuous amorphous phase prior to crystallization, by contrast to previous observations in biominerals.[29] Elucidating nucleation mechanisms by studying synthetic systems, even chemically distant from calcium carbonate or calcium phosphate, but which also show nonclassical nucleation behavior, will certainly prove to be a successful general approach to elucidate pendant questions in biomineralization and address their generic character.

METHODS

Syntheses. All chemicals were used as received. $Eu(NO_3)_3 \cdot 5H_2O$ and $Y(NO_3)_3 \cdot 6H_2O$ were purchased from Aldrich, and the orthovanadate Na_3VO_4 was from Acros (elemental analysis Na: 27.0 wt %, V: 19.9 wt %, C: 3.9 wt %). The Eu-doped YVO_4 nanoparticles are synthesized by an equivolumic mixture of two aqueous precursor solutions: (i) a solution of Y/Eu nitrate in water, with $[Y^{3+}] = 95$ mM and $[Eu^{3+}] = 5$ mM, and (ii) a solution of Na_3VO_4 with a nominal concentration of 100 mM, the pH of which is adjusted to a value of 12.5 by addition of 1 N KOH. The volume of added KOH may be increased in order to decrease the kinetics of the reaction. Upon mixing of both precursors, the clear solution turns white and turbid instantaneously, and the pH decreases to a value of 9.5. After reaction, the colloidal suspension is stabilized by dialysis and subsequent addition of poly(acrylic acid) (PAA 1800, 0.05 mol % of PAA chains with respect to V), which breaks the nanoparticle fractal aggregates through a surface charge increase and yields independent nanoparticles (Figure 1). TiO_2 nanoparticles have been purchased from Crystal Global Company (ref S5-300A). ZrO_2 nanoparticles have been prepared by thermohydrolysis of zirconium acetate as described elsewhere.[6]

Time-Resolved SAXS/WAXS. Time-resolved X-ray scattering patterns with coupled fluorescence spectroscopy have been recorded on the SWING beamline of the SOLEIL synchrotron (Saint-Aubin, France). The range of $q = 1.6 \times 10^{-3}$ Å^{-1} to 2.5 Å^{-1} ($q = 4\pi/\lambda \sin\theta$, with 2θ the angle between the incoming and scattered beam) was obtained with a photon energy of 15 keV and two sample−detector distances of 6.3 m and 58 cm. The sample environment consists of a 3 mm borosilicate glass capillary with two optical fibers coupled to the fluorescence spectrometer. Syntheses have been followed in the time range of $t = 400$ ms to 1 h using two sample injection setups. The shorter reaction times (400 ms < t < 4 s) have been monitored with the lost flow technique: both precursors are injected through a chaotic millifluidic mixer, and the inspected reaction time is determined by the distance between the mixing point of precursors and the X-ray beam and the injection flow rate. Counting times were 10 ms in the SAXS configuration and 100 ms in the WAXS configuration. The longer reaction times (15 s < t < 62 min 15 s) have been inspected with the precursor mixture circulating in close circuit *via* a peristaltic pump between the capillary glass and a reactor. Counting times were 10 ms in the SAXS configuration and 2 s in the WAXS configuration. Steady-state X-ray scattering patterns of the final particles have been recorded in the 1.2×10^{-3} Å^{-1} to 3.2 Å^{-1} range using three complementary homemade setups (copper rotating anode with linear detector on goniometer, or with image plate at 1.2 m, or molybdenum rotating anode with image plate at 73 cm). On all setups, the detector count is normalized to differential cross section per volume unit using water and Lupolen as references. The experimental data have been fitted with the unified equation (Supporting Information 3) using the Matlab software.

Cryo-TEM and HRTEM. Fifty microliters of each precursor solution was mixed in an Eppendorf tube, and after short vortexing, a drop of this solution was deposited on a Quantifoil grid (MicroTools GmbH, Germany). The excess solution was then blotted out with a filter paper, and the grid was quench-frozen in liquid ethane to form a thin vitreous ice film. The delays between the mixing of the precursors and the quenching of the grid were 56 s and 32 min. The grid was then maintained all the time at 96 K to prevent evaporation and crystallization of the ice film. We used a LaB_6 JEOL JEM 2100 (JEOL, Japan) cryo-TEM operating at 200 kV. The images were taken on an ultrascan 2k CCD camera (GATAN, USA) and with a JEOL low-dose system (Minimum Dose System, MDS) to protect the thin ice film from any irradiation before imaging and reduce the irradiation during the image capture. HRTEM observations have been carried out using a JEOL JEM 2100F (JEOL, Japan) equipped with a Schottky emission gun, a UHR pole piece and a Gatan US4000 CCD camera.

Conflict of Interest: The authors declare no competing financial interest.

Acknowledgment. The authors acknowledge C. Chevallard (CEA/SIS2M/LIONS) for stimulating scientific discussions, Olivier Taché and Patrick Haltebourg (CEA/SIS2M/LIONS) for the design of the laboratory WAXS setup, the SOLEIL synchrotron for beam time allocation, and the RTRA-Triangle de la Physique for funding (project 2012-050T Napash).

Supporting Information Available: SAXS/WAXS patterns of other multiscale nanoparticles synthesized in solutions, SAXS/WAXS patterns of the precursor solutions and of their mixture at short times, model used to fit the data, calculated WAXS pattern of YVO_4 and $K_4V_2O_7$ clusters, evolution of the

SAXS/WAXS patterns, and derivation of the nucleation rate from the amorphous-to-crystal conversion. This material is available free of charge *via* the Internet at http://pubs.acs.org.

REFERENCES AND NOTES

1. Alivisatos, A. P. Semiconductor Clusters, Nanocrystals, and Quantum Dots. *Science* **1996**, *271*, 933–937.
2. Hodes, G. When Small Is Different: Some Recent Advances in Concepts and Applications of Nanoscale Phenomena. *Adv. Mater.* **2007**, *19*, 639–655.
3. Jolivet, J.-P. *Metal Oxide Chemistry and Synthesis: From Solution to Solid State*; Wiley: New York, 2000.
4. Privman, V.; Goia, D. V.; Park, J.; Matijević, E. Mechanism of Formation of Monodispersed Colloids by Aggregation of Nanosize Precursors. *J. Colloid Interface Sci.* **1999**, *213*, 36–45.
5. Banfield, J. F.; Welch, S. A.; Zhang, H.; Ebert, T. T.; Penn, R. L. Aggregation-Based Crystal Growth and Microstructure Development in Natural Iron Oxyhydroxide Biomineralization Products. *Science* **2000**, *289*, 751–754.
6. Carriere, D.; Moreau, M.; Barboux, P.; Boilot, J.-P.; Spalla, O. Modification of the Surface Properties of Porous Nanometric Zirconia Particles by Covalent Grafting. *Langmuir* **2004**, *20*, 3449–3455.
7. Corma, A.; Atienzar, P.; García, H.; Chane-Ching, J.-Y. Hierarchically Mesostructured Doped CeO_2 with Potential for Solar-Cell Use. *Nat. Mater.* **2004**, *3*, 394–397.
8. Li, C.; Zhao, Y.; Wang, L.; Li, G.; Shi, Z.; Feng, S. Polyol-Mediated Synthesis of Highly Water-Soluble ZnO Colloidal Nanocrystal Clusters. *Eur. J. Inorg. Chem.* **2010**, *2010*, 217–220.
9. Revaux, A.; Dantelle, G.; Decanini, D.; Haghiri-Gosnet, A.-M.; Gacoin, T.; Boilot, J.-P. Synthesis of YAG:Ce/TiO_2 Nanocomposite Films. *Opt. Mater.* **2011**, *33*, 1124–1127.
10. Becker, R.; Döring, W. Kinetische Behandlung Der Keimbildung in Übersättigten Dämpfen. *Ann. Phys.* **1935**, *416*, 719–752.
11. Vekilov, P. G. Nucleation. *Cryst. Growth Des.* **2010**, *10*, 5007–5019.
12. Gebauer, D.; Völkel, A.; Cölfen, H. Stable Prenucleation Calcium Carbonate Clusters. *Science* **2008**, *322*, 1819–1822.
13. Pouget, E. M.; Bomans, P. H. H.; Goos, J. A. C. M.; Frederik, P. M.; With, G.; de Sommerdijk, N. A. J. M. The Initial Stages of Template-Controlled $CaCO_3$ Formation Revealed by Cryo-TEM. *Science* **2009**, *323*, 1455–1458.
14. Dey, A.; Bomans, P. H. H.; Müller, F. A.; Will, J.; Frederik, P. M.; With, G.; de Sommerdijk, N. A. J. M. The Role of Prenucleation Clusters in Surface-Induced Calcium Phosphate Crystallization. *Nat. Mater.* **2010**, *9*, 1010–1014.
15. Baumgartner, J.; Dey, A.; Bomans, P. H. H.; Le Coadou, C.; Fratzl, P.; Sommerdijk, N. A. J. M.; Faivre, D. Nucleation and Growth of Magnetite from Solution. *Nat. Mater.* **2013**, *12*, 310–314.
16. Reiss, H. The Growth of Uniform Colloidal Dispersions. *J. Chem. Phys.* **1951**, *19*, 482.
17. Wang, X.; Zhuang, J.; Peng, Q.; Li, Y. A General Strategy for Nanocrystal Synthesis. *Nature* **2005**, *437*, 121–124.
18. Sugimoto, T. Underlying Mechanisms in Size Control of Uniform Nanoparticles. *J. Colloid Interface Sci.* **2007**, *309*, 106–118.
19. Weiner, S.; Sagi, I.; Addadi, L. Choosing the Crystallization Path Less Traveled. *Science* **2005**, *309*, 1027–1028.
20. Mialon, G.; Türkcan, S.; Alexandrou, A.; Gacoin, T.; Boilot, J.-P. New Insights into Size Effects in Luminescent Oxide Nanocrystals. *J. Phys. Chem. C* **2009**, *113*, 18699–18706.
21. Pénard, A.-L.; Gacoin, T.; Boilot, J.-P. Functionalized Sol–Gel Coatings for Optical Applications. *Acc. Chem. Res.* **2007**, *40*, 895–902.
22. Casanova, D.; Bouzigues, C.; Nguyen, T.-L.; Ramodiharilafy, R. O.; Bouzhir-Sima, L.; Gacoin, T.; Boilot, J.-P.; Tharaux, P.-L.; Alexandrou, A. Single Europium-Doped Nanoparticles Measure Temporal Pattern of Reactive Oxygen Species Production inside Cells. *Nat. Nanotechnol.* **2009**, *4*, 581–585.
23. Bouzigues, C.; Gacoin, T.; Alexandrou, A. Biological Applications of Rare-Earth Based Nanoparticles. *ACS Nano* **2011**, *5*, 8488–8505.
24. Dantelle, G.; Fleury, B.; Boilot, J.-P.; Gacoin, T. How To Prepare the Brightest Luminescent Coatings? *ACS Appl. Mater. Interfaces* **2013**, *5*, 11315–11320.
25. Huignard, A.; Buissette, V.; Franville, A.-C.; Gacoin, T.; Boilot, J.-P. Emission Processes in YVO_4:Eu Nanoparticles. *J. Phys. Chem. B* **2003**, *107*, 6754–6759.
26. Huignard, A.; Gacoin, T.; Boilot, J.-P. Synthesis and Luminescence Properties of Colloidal YVO_4:Eu Phosphors. *Chem. Mater.* **2000**, *12*, 1090–1094.
27. Beaucage, G. Small-Angle Scattering from Polymeric Mass Fractals of Arbitrary Mass-Fractal Dimension. *J. Appl. Crystallogr.* **1996**, *29*, 134–146.
28. Xia, Y.; Nguyen, T. D.; Yang, M.; Lee, B.; Santos, A.; Podsiadlo, P.; Tang, Z.; Glotzer, S. C.; Kotov, N. A. Self-Assembly of Self-Limiting Monodisperse Supraparticles from Polydisperse Nanoparticles. *Nat. Nanotechnol.* **2011**, *6*, 580–587.
29. Wang, L.; Nancollas, G. H. Calcium Orthophosphates: Crystallization and Dissolution. *Chem. Rev.* **2008**, *108*, 4628–4669.
30. Livage, J. Synthesis of Polyoxovanadates *via* "chimie Douce". *Coord. Chem. Rev.* **1998**, *178–180*, 999–1018.
31. Wallace, A. F.; Hedges, L. O.; Fernandez-Martinez, A.; Raiteri, P.; Gale, J. D.; Waychunas, G. A.; Whitelam, S.; Banfield, J. F.; De Yoreo, J. J. Microscopic Evidence for Liquid–Liquid Separation in Supersaturated $CaCO_3$ Solutions. *Science* **2013**, *341*, 885–889.